Journal of Materials Chemistry A

Accepted Manuscript

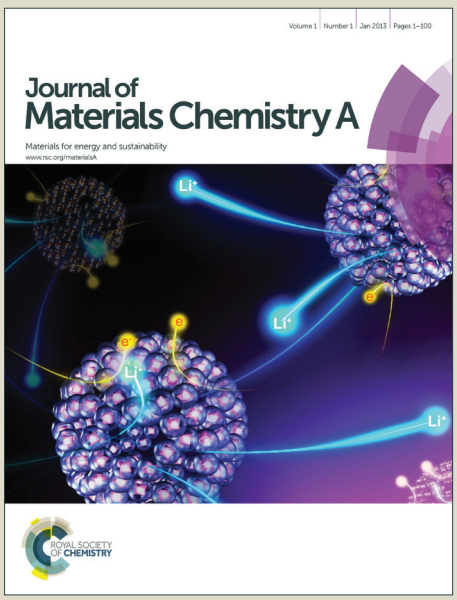

ROYAL SOCIETY OF CHEMISTRY

www.rsc.org/materialsA

Cite this: DOI: 10.1039/c0xx00000x

www.rsc.org/xxxxxx

ARTICLE TYPE

Design of SnO_2/C Hybrid Triple-layer Nanospheres as Li-Ion Battery Anodes with High Stability and Rate Capability

Hao Hu, Haoyan Cheng, Guojian Li, Jinping Liu and Ying Yu*

Received (in XXX, XXX) Xth XXXXXXXXX 20XX, Accepted Xth XXXXXXXXX 20XX

DOI: 10.1039/b000000x

The problem of large volume change during Li insertion and extraction and poor high-power performance for SnO_2-based electrode should be solved for practical application. Herein, a novel SnO_2/C hybrid triple-type nanosphere, in which the layer of amorphous carbon was sandwiched between the layers of SnO_2 and carbon composite, has been designed and fabricated by a top-down approach. Due to the special structure, this kind of SnO_2-based electrode rendered a considerable capacitive performance, offing a greatly enhanced cycling stability and rate capability. Its capacity was kept as high as 653 mAh/g after 350th cycle. The irreversible capacity decay was unprecedentedly extended to 80th cycle. What' more, this electrode even had the capacity of 260 mAh/g at 20C, with a fading of less than 16% after 600 cycles and less than 22% even after 1000 cycles.

Introduction

As lithium ion batteries have been applied in large-scale energy storage areas such as electric cars, power backup, etc., high-performance electrode materials are highly desired. [1-3] Compared with commercial graphite, SnO_2-based electrodes have high reversible specific lithium storage capacity of 990 mAh/g when $Li_{4.4}Sn$ alloys are formed from metallic tin (exception of 710 mAh/g irreversible capacity as decomposition of tin oxide), which is much higher than 372 mAh/g for graphite. However, the Li-metal alloying/de-alloying process enlarges the volume change of electrode materials for more than 200%, which results in the disintegration of conduction pathways between adjacent particles. [4-6]

To address these issues, many efforts have been made to design novel electrode architectures of SnO_2-based anodes. The most common methods are preparing various SnO_2 nanostructures, such as nanoparticles, [7, 8] nanowires, [9, 10] nanosheets, [11] nanotubes, [12-14] nanoboxes, [15] hollow spheres [16, 17] and mesoporous structures [18]. These nanostructures are of great interests due to their special characteristics such as low density, high surface-to-volume ratio, and low coefficients of thermal expansion compared to their solid counterparts. The other frequently-used method is coating stannide with metal, metal oxides or carbon to prevent volume change. [19-23] Stannide and carbon composites has drawn much attention in consideration of price, simple synthesis and synergistic reaction of each component in these materials. Many studies have demonstrated that direct growth of stannide on carbon support could improve the electrical conductivity of the materials, [24, 25] simply coating the stannide with carbon will ease the volume change, [26, 27] and just dispersing tin nanoparticles in carbon may prevent the pulverization and agglomeration of Sn grains upon prolonged cycling. [28-30] However, the development of high-power performance for stannide and carbon composites is still limited. [31-33]

In this study, a novel SnO_2/C hybrid triple-type nanosphere was prepared by changing reaction solvent and temperature (Fig. S1in Support Information). Due to the great difference of diffusion rates for electrons and Li-ions in the middle carbon layer of SnO_2/C hybrid triple-layer nanospheres, the nanosphere may act as a capacitor to promote the reaction of lithium insertion. [32-34] With colloidal carbon sphere as a frame, SnO_2/C hybrid materials can effectively take its advantages of high elastic coefficient and enough space for intrinsic large volume change of transition metal oxides. Moreover, different synthetic structures can be obtained by adjusting the diffusion rate of hydrated metal cations and the adsorption capability of carbonaceous materials.[34] It is worthwhile to note that all the steps in this approach are temperate and scale-producible. The representative synthetic procedure of the SnO_2/C hybrid triple-layer nanospheres (STN), in which the layer of amorphous carbon was sandwiched between the layers of SnO_2 and carbon composite, is illustrated in Scheme 1. Firstly, colloidal carbon spheres were treated with acid to produce more sites for hydrated tin ions to diffuse into carbon frame. Secondly, with the in situ adsorption, stannide can be formed as hydrated tin ions aggregated around the acide sites. [29] Since hydrated tin ions prefer to aggregate on the surface than inside of carbon matrix, [32] stannide would distribute unevenly to form a triple-layer nanosphere structure after diffusion. Finally, the structure of hybrid SnO_2 and partially graphitized carbon was obtained through thermal treatment. The crystallized carbon is believed to transform from amorphous carbon with the catalysis of tin. [33-34] This unique nanostructure and composition with rational design and engineering not only solve the pulverization

problem for

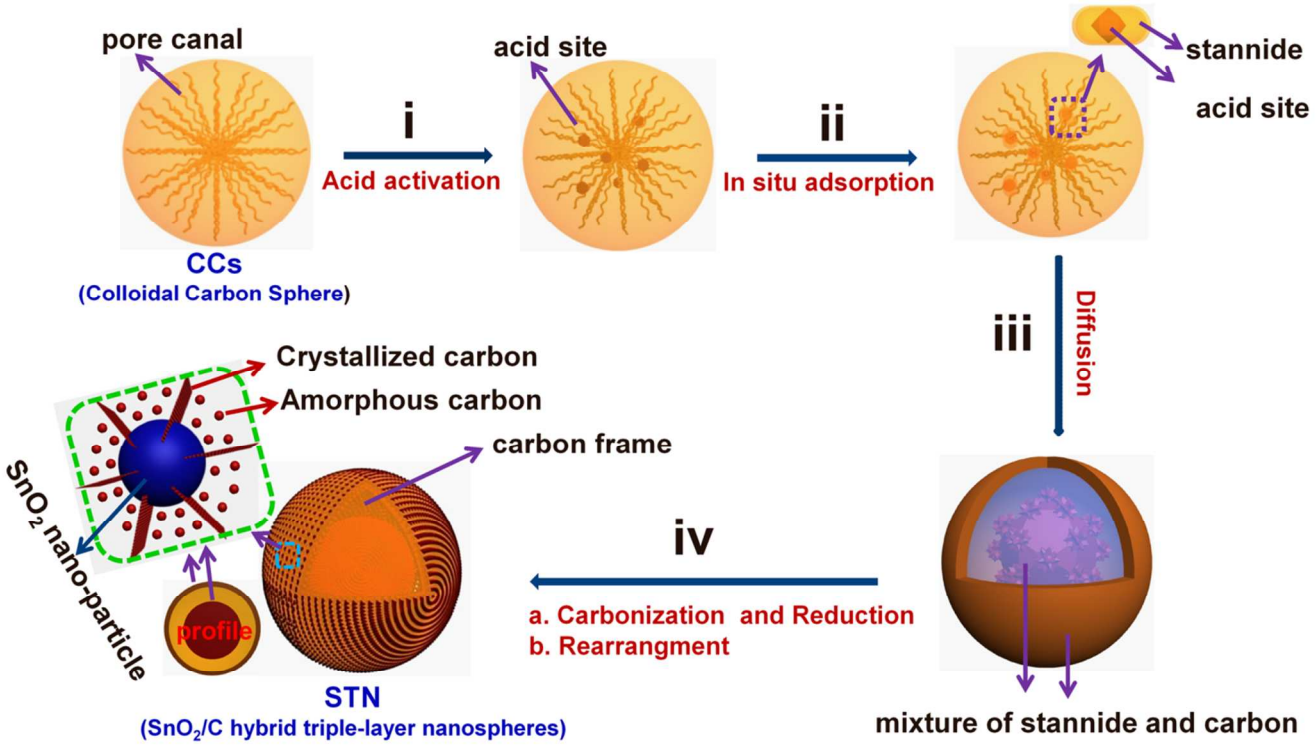

Scheme 1. Schematic illustration of the synthetic procedure and structure details for SnO_2/C hybrid triple-layer nanospheres (STN). i: colloidal carbon spheres were activated with acid to form acid sites; ii: hydrated tin ions were promoted to be adsorbed into carbon frame; ii: the raw of triple-layer nanosphere structure of STN was formed after hydrated tin ions diffusion; iv: STN were prepared after thermal treatment.

SnO_2 anode materials, but also improve high-power lithium-storage performance

Experimental section

Material synthesis

The acidifying colloid carbon spheres were prepared by hydrothermal method in 70 ml (1.2 M) glucose solution at 180 ºC for 5h as reported by Li et al., [35] followed by being treated in 80 ml (1 M) HCl solution at 100°C for 12h. The carbonized colloidal carbon spheres (CCs) were first synthesized through the similar process to the acidifying colloid carbon spheres, and then were carbonized at 500 °C for 3h in argon atmosphere with heating rate of 15 °C/min. Then ultrasonic dispersion of 0.3 g acidifying colloid carbon spheres in 80 mL (water/ethanol = 1:3, v/v) 0.5 M $SnCl_2$ solution and then stirring at 50 °C in a water bath for 8h. The as-prepared products were collected after several rinse-centrifugation cycles. Then, the annealing procedures were first carried out at 500 °C for 3h in N_2 atmosphere with heating rate of 15 °C/min, and then in air at 250 ºC for 1.5h with the rate of 5 °C/min. Thus, SnO_2/C hybrid triple-layer nanospheres were obtained and marked as STN. Next, Pure SnO_2 can be prepared by calcining STN in air at 500 ºC for 2h, which was marked as p-SnO_2. Namely, it was the product after STN was decarbonized. All the reagents were purchased from Sinopharm Chemical Reagent Co., and used without further purification.

Material characterizations

The morphologies and the microstructure of as-prepared samples were characterized with scanning electron microscope (SEM, JSM-6700F, 10 kV), transmission electron microscope (TEM) (JEM-2010FEF, 200 kV) and X-ray diffraction (XRD, X'Pert PRO MRD, PANalytical, Netherlands) with Cu Ka radiation. The nitrogen adsorption–desorption isotherms and the Barrett–Joyner–Halenda (BJH) methods were analysed on a Bel Sorp-mini (S/N-00230) analyzer (accelerated surface area and porosimetry system). X-ray photoelectron spectroscopy (XPS) measurement was performed on a VG ESCALAB 250 spectrometer (Thermo Electron, UK) with monochromatic Al Ka (1486.6 eV) irradiation. Thermogravimetric analysis (TG) was performed with an STA 449C thermal analyser at a heating rate of 15 °C/min in air atmosphere. Raman spectra were recorded at room temperature by virtue of DXR system with 532 nm 8 mW red laser.

Electrochemical measurements

Electrochemical measurements were performed using two electrode CR2016 (3 V) coin-type cells with Li foil as both counter and reference electrodes at ambient temperature. The working electrode consisted of active material, conductivity agent (carbon black, Super-P), and polymer binder (polyvinylidene difluoride, PVDF, Aldrich) in a weight ratio of around 80:5:15. The electrolyte solution was 1 M $LiPF_6$

dissolved in a mixture of ethylene carbonate (EC) and diethyl carbonate (DEC) (1:1 by volume). Cell assembly was performed in an argon-filled glove box (Mbraun, Unilab, Germany) with both moisture and oxygen contents below 1.0 ppm. Galvanostatic charge–discharge tests were performed using a LAND (CT2001A, China) battery testing system in a voltage window of 0.05~2.5V (vs. Li/Li^+). Before testing, the cells were aged for 12h. The cyclic voltammetry (CV) test and EIS measurement was performed on an electrochemical workstation (PARSTAT 2273, Princeton Applied Research, USA) within a voltage range of 0.05~2.5 V and with the frequency range from 100 kHz to 0.01 Hz respectively.

Results and discussion

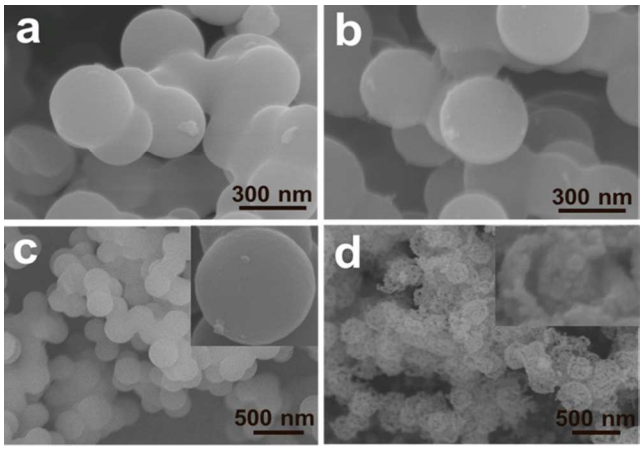

Fig. 1 SEM images of CCs (a), STN before annealing (b), STN (c) and p-SnO_2 (STN after carbon removal) (d).

The morphology of the samples was examined with field-emission scanning electron microscopy (FESEM). Clearly, the carbonized colloidal carbon spheres (CCs) present smooth surface and uniform spherical morphology with diameter of 250 nm (Fig. 1a), while the STN before annealing with a similar diameter but relatively rough surface (Fig. 1b). After thermal treatment, the SnO_2/C hybrid triple-layer nanospheres (STN) (Fig. 1c) shown a rougher surface and same diameter with STN before annealing, further illustrating the structure inheritance during the process. The p-SnO_2 was obtained after the STN annealing in air and calcination led to the removal of carbon for STN. Uniform core-shell structure can be seen in Fig. 1d and the diameter of nanosphere was reduced to 200 nm (Fig. 1d). It can be found that stannide was distributed unevenly inside of the carbon farm, indicating the STN had the nanosphere structure of triple-layer.

The crystal phases of as-prepared samples were recorded by X-ray diffraction (XRD). The results in Fig. 2 unambiguously demonstrate crystal change along with synthetic procedures. Specifically, STN before annealing revealed broad peaks for the poor crystallized phase of SnO_2. Then, the peak of SnO with romarchite structure (JCPDS No. 06-0395) [36] and reflection peak of tetragonal rutile SnO_2 (JCPDS No. 41-1445) appeared after annealing in N_2. [14] Furthermore, the satellite reflection peak at 27.08° may reflect the coupling of tin and carbon. [21, 37] Therefore, the reaction in the process of annealing in N_2 could be described as follow [38].

$$2SnO \rightarrow Sn + SnO_2$$

$$SnO+2C \rightarrow Sn\text{-}(O\text{-})C^* + CO_x \ (1 \leqslant x \leqslant 2)$$

Purity phase of SnO_2 with tetragonal rutile structure (JCPDS No. 41-1445) was observed for the final sample (p-SnO_2). Besides, the broad diffraction peaks around 20~30° were shown in the pattern of naked carbon described as CCs, which were well ascribed to the amorphous carbon. (Fig. S2 in Support Information). [22, 26]

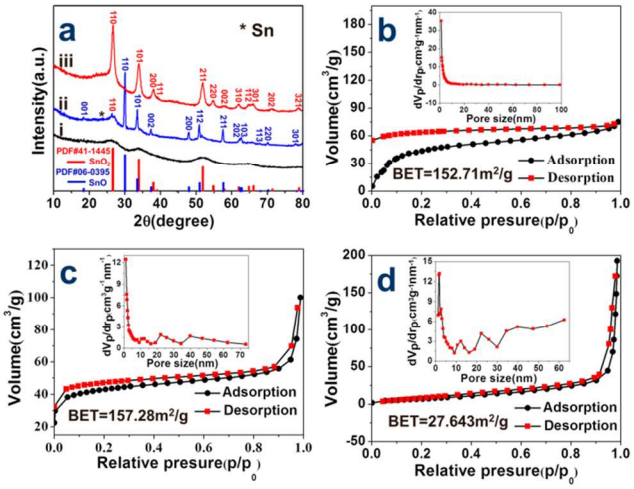

Fig. 2 (a) XRD patterns of STN before annealing (i), STN (ii) and p-SnO_2 (iii); N_2 adsorption–desorption isotherm curves for (b) CCs, (c) STN and (d) p-SnO_2, respectively. (The insets are the BJH pore size distribution).

The surface area and additional pore size distribution information of prepared materials were obtained by N_2 adsorption–desorption isotherm curves. Obviously, the STN (Fig. 2c) revealed a type I isotherm with a type-H4 hysteresis, which was different from the type I isotherms of microporous CCs (Fig. 2b) and mesoporous p-SnO_2 (Fig. 2d). [32] Type-H4 hysteresis and mesopore size distribution suggest that the mesopores in STN may contribute to the space among the particles of STN and the weakly adsorption of N_2 molecules. [23] The surface area of STN was augmented to 172 m^2/g compared with that of 153 m^2/g for CCs. However, the surface area for p-SnO_2 was sharply decreased to 27.6 m^2/g after removing carbon in STN. As a result, the high surface area of STN would contribute to lithium-ions circulation and support the fast sustainable lithium consuming. [32-34]

The transmission electron microscopy (TEM) images of STN shown in Figs. 3a and 3b further verifies that the STN had triple-layer structure with sandwiched carbon as we mentioned before. Moreover, it can be seen that C distribution was relatively uniform in whole nanosphere. Meanwhile, agglomerations of Sn and O were detected in the inner and outer layer of the triple-layer nannosphere from the EDX elemental mapping images of STN (Fig. S3 in Support Information). The difference for Sn and O distribution was caused by the adsorbed oxygen. [28] Additionally, the line-scanning EDX of STN (Fig. S3e in Support Information) showed that the element of C was uniform distributed in the nanospheres, which is in accordance with the results shown in Figs. 3a and 3b. And the three peaks (two sharp

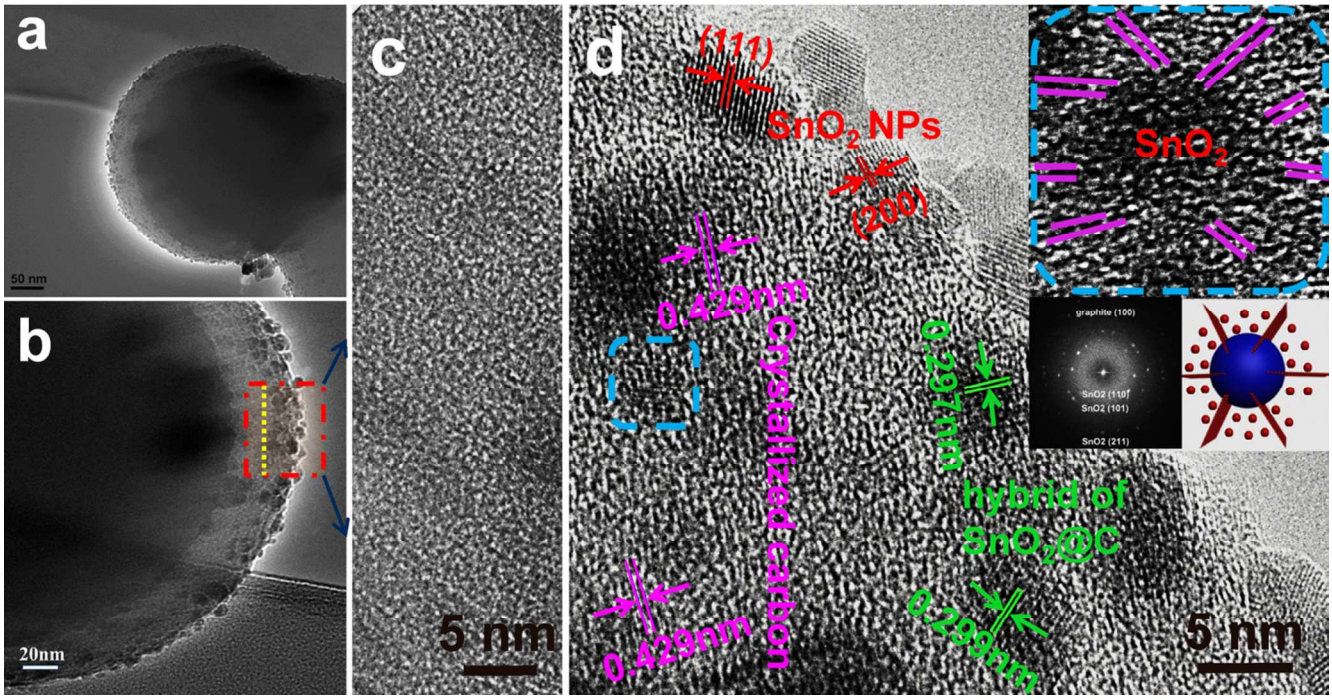

Fig. 3 TEM images of STN (a) and (b), and HRTEM images of the middle layer of STN and the outer layer of STN (d) (insets are detail image of light blue dashed area, its FTT image and the corresponding model.

and one broad) of Sn and O in EDX confirmed that SnO_2 was mainly distributed in the outer and inner of the nanospheres, which indicates that the prepared materials was composed of triple-layer SnO_2/C hybrid nanosphere. In Fig. 3c, the deep focus of HRTEM images on the middle part of STN show that there was amorphous carbon in the middle layer. And in the outer layer of STN as showed in Fig. 3d, it can be found that the vast majority of SnO_2 particles with the size around 5 nm were coated with carbon and distributed uniformly in this layer. The lattice fringes of STN displayed the d space value of 0.231 and 0.237 nm, corresponding to the (111) and (200) plane of SnO_2 respectively.[6, 14, 40] While the value of 0.297 and 0.299 nm agreed with the hybrid of SnO_2 and partially graphitized carbon, and the other wider lattice fringe with the value of 0.429 nm was in accordance with that of graphite.[23, 41, 42] Hence, it is inferred that Sn and carbon may be hybridized, which can contribute to the rearrangement of carbon for the formation of graphitized structure.[22, 41] Moreover, it can be found that the weakly partially graphitized carbon were comprised of interlaced graphitized carbon and amorphous carbon from the inset HRTEM, whose Fast Fourier Transform (FFT) image showed that there was graphite (100) plane.[36] The schematic diagram is shown in the inset of Fig. 3d. This partially graphitized carbon structure may both enhance the stability and increase the lithium-ion diffusion.

To further prove the presence of graphitized structure in STN, we characterized the samples of p-SnO_2 (i), STN (ii), CCs (iii) and commercial graphene (which we suppose it have completely graphitized) (iv) with Raman spectroscopy (Fig. 4) and the data are shown in Fig. 4. Three fundamental Raman scattering peaks were observed at the wavenumbers of 356.7, 627.6 and 759.7 cm^{-1} should be attributed to the E_g Sn-O-Sn vibrational mode, A_{1g} symmetric Sn–O stretching mode and B_{2g} Sn–O vibrational mode, respectively.[22, 26]. Of notice, this result is also in good agreement with tetragonal rutile SnO_2 in STN and p-SnO_2. In our test conditions, the D (1330 cm^{-1}) to G (1580 cm^{-1}) peak intensity ratios higher than 1 for STN and commercial graphene strongly proved that there was graphitized structure, while it was opposite for CCs. [39-41] What' more, just both STN and commercial graphene had a 2D band at 2700 cm^{-1} caused by the double resonant Raman scattering with two-phonon emissions. [44] All of the above indicates that both graphitized carbon and amorphous carbon formed the carbon matrix of STN. [39, 43, 44]

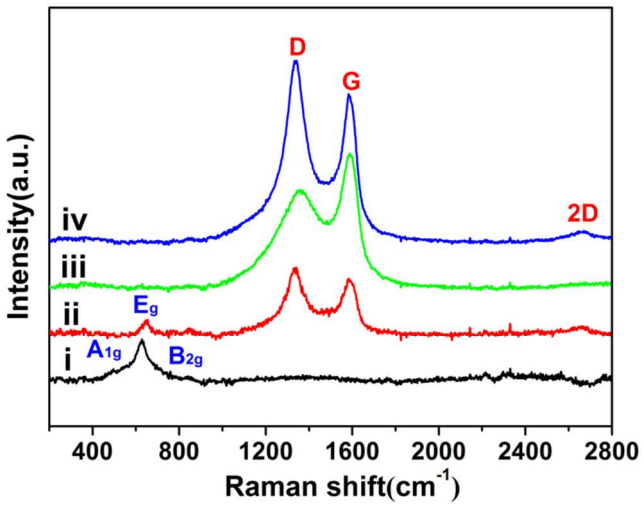

Fig. 4 Raman spectra of p-SnO_2 (i), STN (ii), CCs (iii) and commercial graphene (iv).

XPS was carried out to examine the surface bonding state and the composition of as-prepared STN samples and the

data are shown in Fig. 5. The typical peaks of Sn (3p, 3d, 4s, 4p, 4d) can be observed in survey spectrum (Fig. 5a), which were assigned to SnO_2.[22] The high-resolution spectrum of C 1s in Fig. 5b was split into four peaks corresponding to carbon atoms in different oxygen-containing functional groups. It is indicates that carbon was bonded with tin during the thermal treatment process. The results are in line with Wagner-Meerwein rearrangement reaction.[38, 45, 46] Moreover, it is easy for colloidal carbon which was rich with hydroxyls to form carbon-carbon double bond and hybrid with tin during thermal treatment process.[36, 47] The high-resolution spectrum of the Sn 3d peak shown in Fig. 5c also verifies that bond of C-(O-)Sn was formed.[43] The symmetric peaks centered at 486.98 and 495.43 eV were assigned to Sn-O $3d_{5/2}$ and Sn-O $3d_{3/2}$ respectively, which were characteristic peaks of Sn^{4+} in STN.[48, 49] And the peaks at 487.58 and 495.58 eV were attributed to Sn-(O-)C $3d_{5/2}$ and Sn-(O-)C $3d_{3/2}$ respectively.[50, 51] In Fig. 5d, the O 1s spectrum was composed of three peaks at 533.3, 532.08 and 531.18 eV, which were ascribed to O 1s in O_2, H_2O and O–Sn bonding of STN, respectively.[22, 52] Combined with the results of TEM, Raman and XPS, it can be concluded that the graphitized carbon is partially formed due to the catalysis of metallic tin.

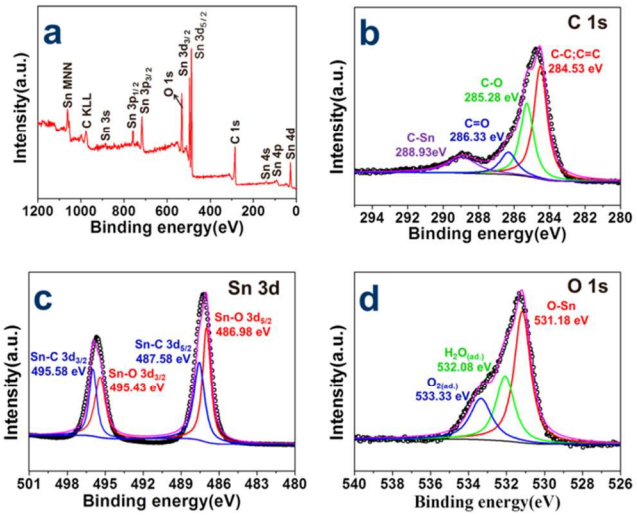

Fig. 5 XPS spectra for STN: a survey spectrum (a) and high-resolution spectra of C 1s (b), Sn 3d (c), and O 1s (d).

We then investigate the electrochemical properties of as-prepared STN, CCs and p-SnO_2 using cyclic voltammetry (CV) and discharge cycling (Fig. 6 and Supporting Information Fig. S5). Perspicuously, the CV for STN was quite different from those for CCs and p-SnO_2 due to the hybrid of carbon and tin. For CCs and p-SnO_2, we can determine that the reduction peak at 0.05 V and the oxidation peak at 0.25 V matched with lithium ion intercalation into and extraction from carbon (equation 1).[16] While the peak around 0.7 V and broad band extending to 0 V corresponded to SnO_2 decomposition (equation 2) and reversible alloying–dealloying reaction (equation 3).[21, 26, 28] Meanwhile, the peak at 1.0 V for STN was ascribed to the formation of SEI layer on the surface of active materials.[41, 54] Interestingly, the band for STN after 50th cycle (Fig. 6d) showed superposition peak of CCs and p-SnO_2, supposing to the formation of stable tunnels for Li-ions diffusion. The carbon content in STN was about 24.22 wt%, which was readily determined by thermogravimetric analysis (TGA) (Fig. S4 in Supporting Information). All of the discharge plateaus (Fig. S5 in Supporting Information) were consistent with the above results. The first and second discharge capacities of STN were 1036 and 845.4 mAh/g. The capacity loss was due to the formation of SEI layer and the decomposition of tin oxide.[35] While the 50th and 100th discharge capacities were all most the same, exhibiting the excellent cycling performance of STN.

$$xLi^+ + C + xe^- \rightarrow Li_xC \quad (1)$$

$$SnO_2 + 4Li^+ + 4e^- \rightarrow Sn + 2Li_2O \quad (2)$$

$$Sn + xLi^+ + xe^- \rightarrow Li_xSn\ (0 \leqslant x \leqslant 4.4) \quad (3)$$

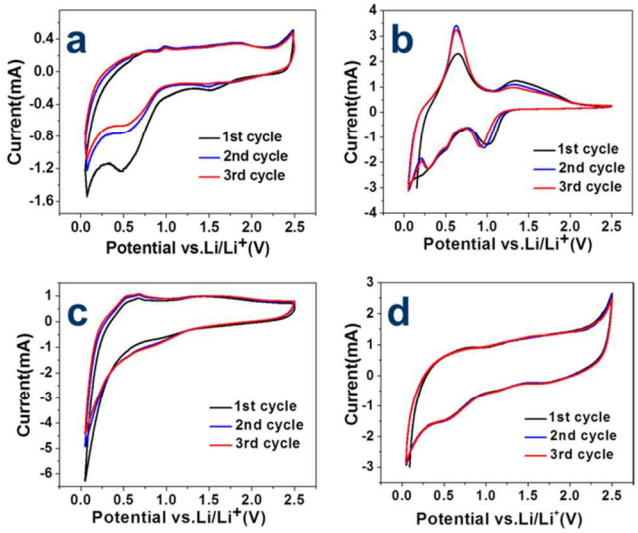

Fig. 6 Cycle voltammogram (CV) profiles of CCs (a), p-SnO_2 (b), STN (c) and the same STN after 50 cycles (d) for the first three cycles between 0.005 and 2.5 V at a scan rate of 0.5 mV s^{-1}.

As expected, the STN hybrid electrode demonstrates much more stable cycling performance than p-SnO_2 electrode. Its capacity kept as high as 653 mAh/g after 350th cycle (Fig. 7). Therefore, the irreversible capacity decay, which can be calculated from the data in Fig. S5, was unprecedentedly extended to 80th cycle. It is much better than those previously reported from nanostructures fabrication of SnO_2 and carbon composites (Table S1 Support Information). Additionally, the SEM images of STN shown in Fig. S6a (Supporting Information) revealed that 350 cycles did not change the main morphology. Whereas the capacity of the composite of SnO_2@carbon nanotubes (CNT) (Fig. S7 in Supporting Information) was rapidly decreased from 1165 to 542 mAh/g after five cycles. It indicates that the irreversible capacity of SnO_2 decomposition can be improved when apt condition was provided, as inferred before.[26, 54-56] For p-SnO_2, the capacity decay was a spectacular disappointment that it was decayed nearly to zero after 124th cycle, following the poor cyclability and large volume change for transitional metal oxide materials.[25, 44] Substantially, the

special hybrid structure of STN was effective to avoid the large volume change for electrode materials during Li insertion and extraction.

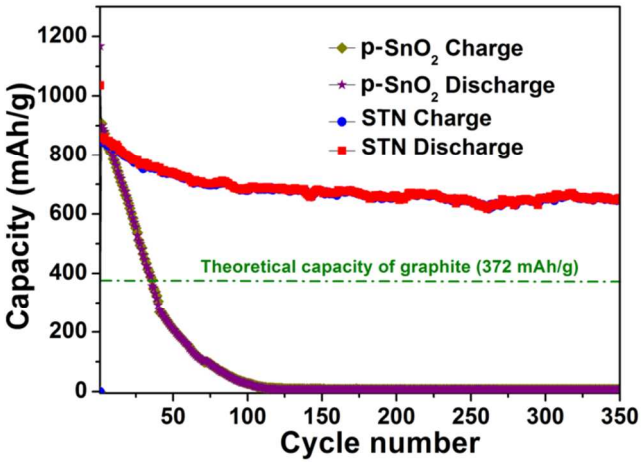

Fig. 7 Cycling performance of STN and p-SnO_2 electrodes at a current density of 300 mA/g with voltage window of 0.05 V~2.5 V.

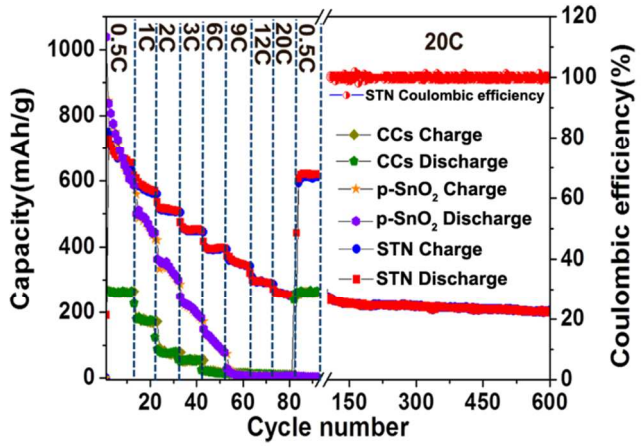

Fig. 8 Rate performance of STN (C = 690 mA/g), p-SnO_2 (C = 990 mA/g) and CCs (C = 372 mA/g) electrodes at various current rates.

Moreover, the prepared materials also showed remarkable high power rate capability at 0.5~20 C as presented in Fig. 8. Compared with p-SnO_2 and CCs, STN demonstrated excellent cyclability whose capacity was more than 2.5 times as that of CCs at different rates and its rate advantage was predominant especially at high rates. At different current rate of 0.5, 1, 2, 3, 6, 9, 12 and 20 C, the reversible capacities of STN were around 680, 590, 510, 450, 400, 360, 300 and 260 mAh/g, respectively. And the capacity of the materials became stable and reversible after initial few cycles. What's more, the capacity still remained around 610 mAh/g at 0.5 C after 80 cycles, which was just 90% of the capacity at 0.5 C in the initial ten cycles. It's worth noting that the fade was less than 16% at 20 C after 600 cycles and less than 22% even after 1000 cycles (Fig. S8 in Supporting Information). The morphology of STN after 1000th cycle at 20 C was imaged and the results are shown in Fig. S6b (Supporting Information). As we can see, the nanosphere structure for STN electrode after 1000th cycle at 20 C was almost maintained but the cycling process also made the surface coarser compared with that for STN before cycling as shown in Fig. 1b, further illustrating the structure inheritance.

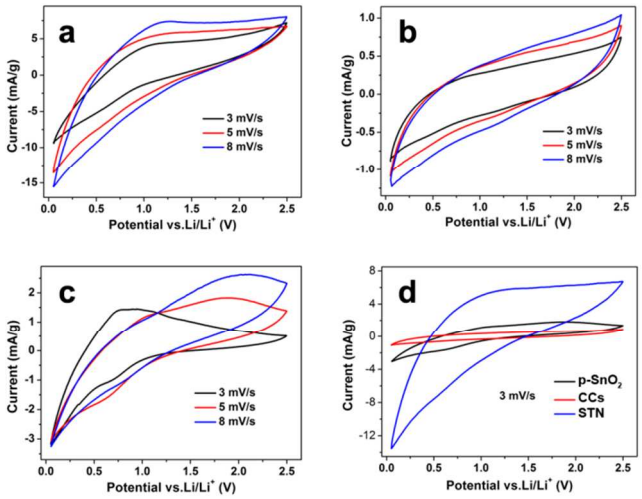

Fig. 9 Cyclic voltammograms of STN (a), CCs (b), p-SnO_2 (c) at different scan rates and the comparison for p-SnO_2, CCs, STN at 3 mV/s (d).

To further confirm the capacitance characteristic for the high-power performance of STN, cyclic voltammograms (CV) with different scan rates were performed and the results are displayed in Fig. 9. The capacitance (F/g) can be calculated from the following equation:

$$C = \frac{\int_{V_0}^{V_0+\Delta V} J dV}{s\Delta V}$$

where J is the current density (A/g), s the voltage scan speed (V/s), V_0 the initial voltage and ΔV the voltage window (V) for the cycling test. [57] Based on this equation, the sample of STN had a pseudocapacitance performance feature with maximal integrated area (1.14 F/g). For CCs and p-SnO_2, tiny integrated areas at the same scan rate indicated pimping capacitive performance. Besides, the capacities of p-SnO_2 and CCs approach to zero at high rate (Fig. 8, current rate higher than 9C) and the symmetrical prolongation CV curves may be caused by polarization with increasing voltage scan speed. [43-45] So, the capacitance characteristic of STN indicates the higher-power performance than that of CCs and p-SnO_2. Additionally, EIS measurement was performed as show in Fig. S9, the impedance spectra were recorded for the electrodes at the first and 100th cycles. Compared with CCs and p-SnO_2 electrode, the STN electrode had lower resistance and higher lithium-ion mobility, especially after 100th cycle. Moreover, the STN electrode was not only different from the p-SnO_2 electrode which with two semicircles due to structure change but also different from the CCs electrode with the decreased linear slope of Warburg impedance at the low frequency region for lithium-ion accumulation and consumption in the interstice of the structure.[37, 48] To some degree, the diameter of tin dioxide particles in STN was almost 5 nm and the hybrid with partially graphitized carbon can mitigate the absolute strain induced by the large volume change during lithiation/delithiation, and thereafter retard particle pulverization. Moreover, the key point is that the unique structure can be stable during lithiation/delithiation because of the high

spring constant of partially graphitizied carbon and the tripe-layer structure may lead to a capacitive performance, which is beneficial for lithium-ion to migrate fast.

The stabilized cycling performance and high rate capability of STN can be attributed to the rational design and engineering of the unique nanostructure and composition. As illustrated in Scheme 2, the triple-layer structure with sandwiched carbon has a capacitive performance to improve the high-power performance of STN. Additionally, the partially graphitized carbon in the mixture layers of STN may be responsible for the stability enhancement since it could be compressed while the volume of SnO_2 swelled during lithium insertion. Moreover, the partially graphitized carbon may act as the keels for SnO_2 to keep the structure stable and the partial amorphous carbon with more incompact lattice spacing can promote the lithium-ion diffusion compared with graphitized carbon. All of the above synergistic lead to addressing the pulverization issue for SnO_2 anode materials and improving lithium-storage properties. It is worth mentioning that the discharge performance of irreversible (decomposition of tin oxide) and high-power performance of STN are substantially enhanced because of their unique structures and rational hybrid of composition compared with many other SnO_2 nanostructures (Table S1 in Supporting Information).[22, 26, 54] The design of STN offers another promising route for the improvement of the cycling life of electrode materials with large volume change.

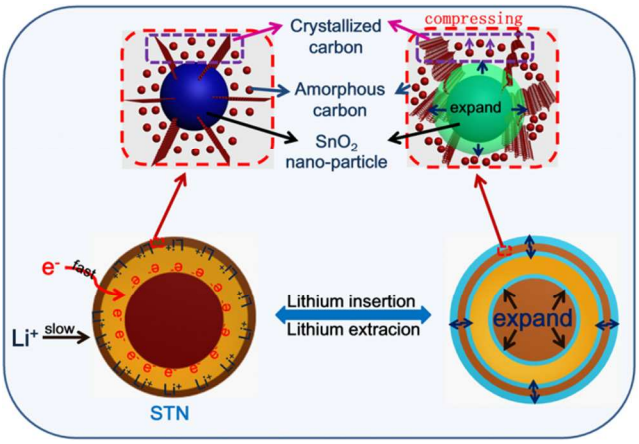

Scheme 2. Schematic illustrated the stability of STN while lithium insertion and extraction.

Conclusions

Novel hybrid composite of SnO_2/C hybrid triple-type nanosphere have been successfully prepared by a top-down approach. The sandwiched carbon layer acts as physical buffer for intrinsic large volume change. Moreover, the hybrid of tin and partially graphitized carbon can consolidate structure protection, and improve electron transfer and lithium-ion diffusion. As a result, the electrochemical property of the STN electrode is largely enhanced with highly stable cycling and high-power charge/discharge performance. Additionally, the discharge performance decay of irreversible capacity (decomposition of tin oxide) is alleviated. The electrode material design and the temperate and scale-producible technology in this work, which ingeniously uses top-down method to combine the nanostructure and rational hybrid of different components, can be applicable for other electrode materials with high electrochemical performance.

Acknowledgements

This work was financially supported by National Science Foundation of China (No. 21377044), Wuhan Planning Project of Science and Technology (No. 2014010101010023) and self-determined research funds of CCNU from the colleges' basic research and operation of MOE (No. CCNU13F027).

Notes and references

[a] *Institute of Nanoscience and Nanotechnology, College of Physical Science and Technology, Central China Normal University, Wuhan 430079, P.R. China.*
[b] ** Corresponding author. Tel: 86-27-67867037; Email: yuying01@mail.ccnu.edu.cn.*

Electronic Supplementary Information (ESI) available: [SEM and TEM images for STN sythesis in other conditions; XRD pattern of naked carbon; DF-STEM image, elemental mapping images and line-scanning EDX mapping data for STN; TGA curve of STN, discharge voltage profiles of STN for different cycles at current density of 300 mA/g, SEM images of STN electrode after 350th cycle; SEM images, XRD pattern and cycling performance of SnO_2@CNT; cycling performance of STN at a current rate of 20 C and summary of the discharge performance for variously typical SnO_2-based anodes. SEM images of STN electrodes after 350th cycle at 300 mA/g and after 1000th cycle at 20 C; Nyquist plots of CCs, STN and p-SnO_2 electrodes. Summary of the discharge performance (irreversible and reversible capacity) for variously typical SnO_2-based anodes.]. See DOI: 10.1039/b000000x/

1 A. Patrice, G. Yury, *Nat. Mater.*, 2008, **7**, 845-854.
2 K. T. Nam, D. W. Kim, P. J. Yoo, C. Y. Chiang, N. Meethong, P. T. Hammond, Y. M. Chiang, A. M. Belcher, *Science.*, 2006, **312**, 885-888.
3 A. Magasinsk, P. Dixon, B. Hertzberg, A. Kvit, J. A. Yushin, G. Yushin, *Nat. Mater.*, 2010, **9**, 353-358.
4 L. Zhang, G. Zhang, H. B. Wu, L. Yu,; X. W. Lou, *Adv. Mater.*, 2013, **25**, 2589-2593.
5 H. Zhang, X. C. Feng, Y. C. Zhai, K. L. Jiang, Q. Q. Li, S. S. Fan, *Adv. Mater.*, 2009, **21**, 22992304.
6 H. Zhang, H. Song, X. Chen, J. Zhou, H. J. Zhang, *Electrochim. Acta.*, 2012, **59**, 160-167.
7 L. Cui, J. Shen, F. Cheng, Z. Tao, J. S. Chen, *J. Power Source.*, 2011, **196**, 2195-2201.
8 K. Chunjoong, N. Mijung, C. Myungsuk, C. Jaephil, P. Byungwoo, *Chem. Mater.*, 2005, **17**, 3297-3301.
9 Z. Cai, J. Li, *Ceramics International.*, 2013, **39**, 377-382.
10 B. Cheng, C. Xie, L. Fang, Y. Xiao, S. Lei, *Mater. Chem. Phys.*, 2011, **129**, 713-717..
11 C. Wang, Y. Zhou, M. Ge, X. Xu, Z. Zhang, J. Z. Jiang, *J. Am. Chem. Soc.*, 2010, **132**, 46-47.
12 Y. Wang, H. C. Zeng, J. Y Lee, Adv. Mater. 2006, **18**, 645-649.
13 J. Ye, H. Zhang, R. Yang, X. Li, L. Qi, *Small.*, 2010, **6**, 296-306.
14 X. Zhang, J. Liang, G. Gao, S. Ding, Z. Yang, W. Yu, B.Q. Li, *Electrochim. Acta.*, 2013, **98**, 263-267.
15 Z. Wang, D. Luan, F. Y. Boey, X. W. Lou, *J. Am. Chem. Soc.*, 2011, **133**, 4738-4741.

16 X. W. Lou, Y. Wang, C. Yuan, J. Y. Lee, L. A. Archer, *Adv. Mater.*, 2006, **18**, 2325-2329.
17 W. S. Kim, Y. Hwa, J.H. Jeun, H. J. Sohn, S.H. Hong, *J. Power Source.*, 2013, **225**, 108-112.
18 Z. Wen, Q. Wang, Q. Zhang, J. Li, *Adv. Funct. Mater.*, 2007, **17**, 2772-2778.
19 J. S. Chen, D. Luan, C. M. Li, F. Y. Boey, S. Qiao, X. W. Lou, *Chem. Commun.*, 2010, **46**, 8252-8254.
20 L. B. Chen, X. M. Yin, L. Mei, C. C. Li, D. N. Lei, M. Zhang, Q. H. Li, Z. Xu, C. M. Xu, T. H. Wang, *Nanotechnology.*, 2012, **23**, 035402.
21 S. Ding, J. S. Chen, X. W. Lou, *Chem. Asian J.*, 2011, **6**, 2278-2281.
22 M. He, L. Yuan, X. Hu, W. Zhang, J. Shu, Y. Huang, *Nanoscale.*, 2013, **5**, 3298-3305.
23 K. T. Lee, J. C. Lytle, N. S. Ergang, S. M. Oh and A. Stein, *Adv. Funct. Mater.*, 2005, **15**, 547-556.
24 L. Ji, Z. Lin, B. Guo, A. J. Medford, X. Zhang, *Chem. Eur. J.*, 2010, **16**, 11543-11548.
25 H. Liu, J. Huang, X. Li, J. Liu,. X. Zhang, *Ceram. Int.*, 2012, **38**, 5145-5149.
26 X. W. Guo, X. P. Fang, Y. Sun, L. Y. Shen, Z. X. Wang, L. Q. Chen, *J. Power Source*, 2013, **226**, 75-81.
27 X. W. Lou, J. S. Chen, P. Chen, L. A. Archer, *Chem. Mater.*, 2009, **21**, 2868-2874.
28 Y. Xu, Q. Liu, Y. Zhu, Y. Liu, A. Langrock, M. R. Zachariah, C. Wang, *Nano Lett.*, 2013, **13**, 470-474.
29 G. Derrien, J. Hassoun, S. Panero and B. Scrosati, *Adv. Mater.*, 2007, **19**, 2336-2340.
30 J. Hassoun, G. Derrien, S. Panero and B. Scrosati, *Adv. Mater.*, 2008, **20**, 3169-3175.
31 H. B. Wu, J. S. Chen, H. H. Hng and X. W. Lou, *Nanoscale*, 2012, **4**, 2526-2542.
32 L. Zhang, G. Zhang, H. B. Wu, L. Yu and X. W. Lou, *Adv. Mater.*, 2013, **25**, 2589-2593.
33 J. Wang, W. Li, F. Wang, Y. Xia, A. M. Asiri and D. Zhao, *Nanoscale*, 2014, **6**, 3217-3222.
34 J. Wang, N. Yang, H. Tang, Z. Dong, Q. Jin, M. Yang, D. Kisailus, H. Zhao, Z. Tang, D. Wang, *Angew. Chem. Int. Ed.*, 2013, **52**, 1 – 5.
35 X. Sun and Y. Li, *Angew. Chem.*, 2004, **116**, 607-611.
36 A. Doron, N. Alex, M. Boris, L. Elena, S. Elena and G. Aharon, *Chem. Mater.*, 2002, **14**, 4155-4163.
37 L. Chen, Z. Wang, C. He, N. Zhao, C. Shi, E. Liu and J. Li, *ACS Appl. Mater. Interfaces*, 2013, **5**, 9537-9545.
38 A. Julio, M. Rodrı´guez, P. H. Cuong and B. Florian, *ACS Nano*, 2011, **5**, 1529–1534.
39 E. Scott and F. N.Linda, *Acc. Chem. Res.*, 2013, **46**, 1135-1143.
40 X. Chen, K. Kierzek, K. Wilgosz, J. Machnikowski, J. Gong, J. Feng, T. Tang, R. J. Kalenczuk, H. Chen, P. K. Chu and E. Mijowska, *J. Power Source.*, 2012, **216**, 475-481.
41 Y. Fang, Y. Lv, R. Che, H. Wu, X. Zhang, D. Gu, G. Zheng and D. Zhao, *J. Am. Chem. Soc.*, 2013, **135**, 1524-1530.
42 J. Liu, J. Huang, L. Hao, H. Liu and X. L. Li, *Ceram. Int.*, 2013, **39**, 8623-8627.
43 U. B. Suryavanshi and C. H. Bhosale, *J. Alloy. Compd.*, 2009, **476**, 697-704.
44 M. S. Park, G. X. Wang, Y. M. Kang, D. Wexler, S. X. Dou and H. K. Liu, *Angew. Chem.*, 2007, **119**, 764-767.
45 A. O.George, *Acc. Chem. Res.*, 1976, **9**, 41-52.
46 R. L., T. E. Cargill, Jackson and N. P. P. a. D. M. P., *Acc. Chem. Res.*, 1974, **7**, 106-113.
47 S. Ding, J. S. Chen and X. W. Lou, *Chem. Asian J.*, 2011, **6**, 2278-2281.
48 X. W. Lou, C. M. Li and L. A. Archer, *Adv. Mater.*, 2009, **21**, 2536-2539.
49 L. Wang, D. Wang, Z. Dong, F. Zhang and J. Jin, *Nano lett.*, 2013, **13**, 1711-1716.
50 B. Chen, H. Qian, J. Xu, L. Qin, Q.-H. Wu, M. Zheng and Q. Dong, *J. Mater. Chem. A.*, 2014, **2**, 9345-9350.
51 X. Wang, X. Cao, L. Bourgeois, H. Guan, S. Chen, Y. Zhong, D.-M. Tang, H. Li, T. Zhai, L. Li, Y. Bando and D. Golberg, *Adv. Fun. Mater.*, 2012, **22**, 2682-2690.
52 É. P. Domashevskaya, S. V. Ryabtsev, S. Y. Turishchev, V. M. Kashkarov, Y. A. Yurakov and O. A. C. a. A. V. Shchukarev, *J. Struct. Chem.*, 2008, **49**, S80-S91.
53 X. W. Lou, C. M. Li and L. A. Archer, *Adv. Mater.*, 2009, **21**, 2536-2539.
54 S. Ding, J. S. Chen and X. W. Lou, *Chem. Asian J.*, 2011, **6**, 2278-2281.
55 N. S. Choi, Z. Chen, S. A. Freunberger, X. Ji, Y. K. Sun, K. Amine, G. Yushin, L. F. Nazar, J. Cho and P. G. Bruce, *Angew. Chem. Int. Ed.*, 2012, **51**, 9994-10024.
56 Y. Xu, Q. Liu, Y. Zhu, Y. Liu, A. Langrock, M. R. Zachariah and C. Wang, *Nano Lett.*, 2013, **13**, 470-474.
57 L. Huang, D. Chen, Y. Ding, S. Feng, Z. L. Wang, and M. Liu, *Nano Lett.*, 2013, **13**, 3135 −3139.

Schematic illustration of the unique nanostructure and composition of STN for alleviating the pulverization problem as SnO_2 anode materials and its superior electrochemical performance